

Theoretical Investigation of Strain-Adjustable $\text{Ge}_{0.92}\text{Sn}_{0.08}$ Light-Emitting Diodes With Giant Magnetostrictive Stressor for Short-Wave Infrared Light Source

Qingfang Zhang , Qianyu Chen , Jitao Zhang , Wenxiang Lu, Pei Zhang , Zirui Qin, Lingzhi Cao, and Genquan Han

Abstract—A new idea was provided by the group-IV GeSn alloys for short-wave infrared light source compatible with CMOS due to the low cost integrated on the Si platform and can be transformed into direct bandgap alloy. More than 7.1% Sn content or strain engineering is used to achieve the direct bandgap GeSn semiconductors and enhance the luminous efficiency of GeSn light-emitting devices. We theoretically investigate a strain-adjustable GeSn light-emitting diode with the giant magnetostrictive stressor. A 0~0.11% adjustable uniaxial tensile strain is introduced into $\text{Ge}_{0.92}\text{Sn}_{0.08}$ LED by adjusting the external magnetic field. A continuously adjustable bandgap from 0.543 eV to 0.475 eV of the $\text{Ge}_{0.92}\text{Sn}_{0.08}$ alloy is achieved in the magnetic field intensity range of 0~240 kA/m, and the spontaneous emission rate of the strained LED is enhanced about 3.63 times compared with the relaxed device. Besides, an adjustable range of luminous peak is achieved from 2.18 μm to 2.46 μm , which can promote the application of GeSn light source for magnetic field detection and photo-communication in short-wave infrared.

Index Terms—Adjustable tensile strain, GeSn alloys, giant magnetostrictive stressor, LED.

I. INTRODUCTION

UNDER the constraints of Moore's Law, the integration level of integrated circuits continues to increase, the size of devices gradually decreases, and the physical limitation of

Manuscript received 28 November 2022; revised 27 December 2022; accepted 26 January 2023. Date of publication 31 January 2023; date of current version 10 February 2023. This work was supported in part by the National Natural Science Foundation of China (NSFC) under Grants 62004177, 61973279, 12004348, and 52005454, in part by the Foundation of Outstanding Young Scholars in Henan Province under Grant 222300420096, in part by the Foundation for University Young Backbone Scholars in Henan Province under Grant 2020GGJS122, in part by the Project of Central Plains Science and Technology Innovation Leading Talents under Grant 224200510026, and in part by the Key Scientific Research Project Plan of Universities in Henan Province under Grant 20A510015. (*Corresponding authors:* Qingfang Zhang; Jitao Zhang.)

Qingfang Zhang, Qianyu Chen, Jitao Zhang, Wenxiang Lu, Pei Zhang, Zirui Qin, and Lingzhi Cao are with the School of Electrical and Information Engineering, Zhengzhou University of Light Industry, Zhengzhou 450002, China (e-mail: qingfang@zzuli.edu.cn; 2018829@zzuli.edu.cn; zhangjitao@zzuli.edu.cn; luwenxianglw@outlook.com; zhangpei@zzuli.edu.cn; qinrz@zzuli.edu.cn; caolinqzhi@zzuli.edu.cn).

Genquan Han is with the School of Microelectronics, Xidian University, Xi'an 710071, China, and also with the Hangzhou Institute of Technology, Xidian University, Hangzhou 311200, China (e-mail: hangenquan@gmail.com).

Digital Object Identifier 10.1109/JPHOT.2023.3240828

electrical connections between devices in integrated circuits begins to appear. Silicon-based optoelectronics can overcome the interconnect bottlenecks facing modern integrated circuits (ICs) [1], [2], [3]. Compared with the typical Si-based Photonic Integrated Circuit (PIC) lattice-matched light source composed of III-V (AlP, GaP, AlAs, GaAs) and II-VI (ZnSe) materials whose emission wavelength are distributed in the visible spectrum (400–900 nm). Group-IV GeSn is compatible with CMOS processes and can be transformed into direct bandgap alloy, which is the promising material for short-wave infrared (SWIR) light source [4], [5]. The Γ valley decreases faster than the L valley with the increase of introduced Sn, and the indirect-to-direct transition will be realized when Sn content reaches 7.1% [6], [7], [8], [9], which can extend the applications such as electro-magnetic spectrum -based night vision and the optic window for the transcranial light [10], [11], [12], [13]. However, it is difficult to increase the Sn content by more than 14% for light source material due to the Sn segregation caused by the low solid solubility (<1%) of Sn in Ge and the large lattice mismatch [14], [15].

To avoid the growth defects caused by merely increasing the Sn content, strain engineering was taken to realize the indirect to direct bandgap transition of GeSn alloys [16], [17], [18]. A significant improvement of the luminous efficiency and wavelength application in the mid-infrared spectra with the tensile stressor [10], [19]. A 2.5% Sn composition for the conversion of GeSn alloy from indirect bandgap to direct bandgap was realized with the fixed biaxial tensile strain of about 0.76% introduced by a 300 nm Si_3N_4 liner stressor in our previous studies of the light-emitting device (LED) based on GeSn material [20].

In order to satisfy the application of the adjustable light source for photo-communication and sensor, the adjustable stressor is investigated. With the development of magneto-optical materials, the giant magnetostrictive materials were used as the excellent adjustable stressor for the fast response speed and large output force [21]. A magnetostrictive deformation over 2000 ppm (10^{-6}) can be achieved under the magnetic field strength of 200 kA/m with a uniaxial pre-stress of about 24 MPa [22], [23].

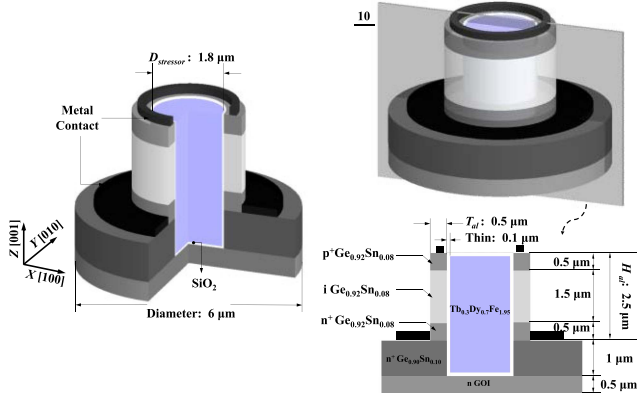


Fig. 1. 3D schematic diagram of $\text{Ge}_{0.92}\text{Sn}_{0.08}$ LED with a giant magnetostrictive stressor. The key geometric and material parameters are shown in Fig. 1. The $10'$ plane cuts through the GeSn LED along $[100]$ direction.

In our research group, by changing the doping concentration and the shape of the magnetostrictive material, the non-reciprocal current–voltage conversion efficiency has been increased by about 33% and up to 91.3% at the load $R_L = 25.6 \text{ k}\Omega$ [24], [25]. In this letter, a novel strained GeSn LED with a giant magnetostrictive stressor is proposed and investigated theoretically. An adjustable tensile strain is introduced in the active layer along the direction of the magnetic field by the stressor to reduce the $E_{G,\Gamma}$ of GeSn, which leads to the improvement of light emission efficiency of the device and the extension of wavelength in SWIR. Comparison studies of energy band structures and light emission efficiency of relaxed and tensile strained GeSn LEDs with various magnetic fields are carried out.

II. DESIGN OF DEVICE STRUCTURE

Fig. 1 shows the schematic of p^+ -i- n^+ $\text{Ge}_{0.92}\text{Sn}_{0.08}$ LED with a giant magnetostrictive stressor grown on an n^+ $\text{Ge}_{0.90}\text{Sn}_{0.10}$ relaxed layer, which was designed and optimized theoretically based on the strain simulations and the experimental reports. The cross-sectional $10'$ cuts through the center line along $[100]$ of the GeSn LED. $\text{Ge}_{0.92}\text{Sn}_{0.08}$ was chosen as the active layer to ensure the bottom of the conduction band and the top of the valence band at the same k point [9]. Line defects and compressive strain in the active layer induced during the growth process of $\text{Ge}_{0.92}\text{Sn}_{0.08}$ can be reduced by the larger Sn content $\text{Ge}_{0.90}\text{Sn}_{0.10}$ in the relaxed layer [14], [26], [27]. All layers except the substrate are etched by dry etching into a hollow cylinder with an outer diameter of $6 \mu\text{m}$ and an inner diameter of $2 \mu\text{m}$ [28]. A layer of SiO_2 insulating thin film is deposited on the inside of the hollow cylinder by chemical vapor deposition (CVD) to play the role of passivation, which can eliminate the influence on the carriers lifetime [29], and the giant magnetostrictive material is filled into the hollow cylinder structure by magnetron sputtering process as a strain source [30], [31]. Then, the active layer is etched into a cylinder with an outer diameter of $3 \mu\text{m}$. Finally, the metal electrodes are prepared

TABLE I
GEOMETRIC PARAMETERS AND MATERIALS PROPERTIES USED IN SIMULATION OF STRAIN PROFILES

Active layer Height $H_{al} (\mu\text{m})$	Active layer Thickness $T_{al} (\mu\text{m})$	$\text{Tb}_{0.3}\text{Dy}_{0.7}\text{Fe}_{1.95}$ Diameter $D_{stressor} (\mu\text{m})$	Young's modulus (GPa)		
			Ge	α -Sn	$\text{Tb}_{0.3}\text{Dy}_{0.7}\text{Fe}_{1.95}$
5	1	1.8	102.9[36]	51.5[36]	50[37]

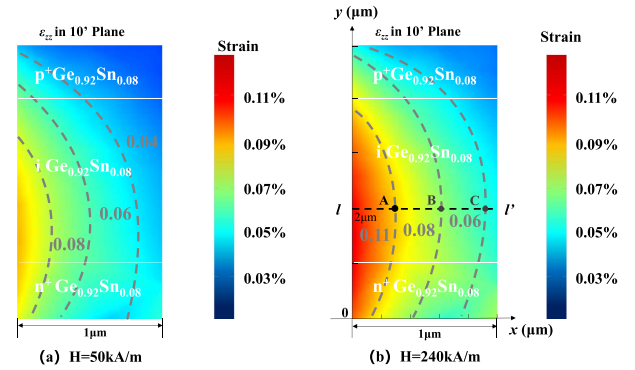


Fig. 2. The $10'$ plane cuts through the GeSn LED along $[100]$ direction. Uniaxial tensile strain contour distribution in ε_{zz} along $[001]$ direction on the $10'$ plane in p^+ -i- n^+ of GeSn LED structure under different magnetic fields (a) $H = 50 \text{ kA/m}$, (b) $H = 240 \text{ kA/m}$.

by metal contact deposition with a lift-off process [32], [33]. $\text{Tb}_{0.3}\text{Dy}_{0.7}\text{Fe}_{1.95}$ belongs to the ternary Laves phase with lower magneto crystalline anisotropy and higher magnetostriction coefficient (λ) which can be used as the adjustable stressor [34], [35], [36]. In the absence of external stress, the magnetostriction coefficient will increase accordingly by adjusting the strength of the external magnetic field (H) until saturation, up to 1200 ppm [37].

III. RESULT AND DISCUSSION

A. Simulation of Strain Profiles in Active Layer of GeSn LED

A 3D Finite Element Method (FEM) simulation was performed to analyze the effect of the $\text{Tb}_{0.3}\text{Dy}_{0.7}\text{Fe}_{1.95}$ stressor on the active layer of GeSn LED. The geometric parameters and material properties used in simulations are listed in Table I. Young's modulus of GeSn was calculated by linear interpolation method based on the values of Ge and α -Sn [38], [39]. We assumed that Young's modulus of the materials is isotropic, and the directed values were utilized. The saturated magnetostriction coefficient of $\text{Tb}_{0.3}\text{Dy}_{0.7}\text{Fe}_{1.95}$ was set as 1200 ppm. The boundary conditions of the model were set as follows, the bottom surface of the GOI substrate was fixed with zero displacements in any direction, and other surfaces were set to be free surfaces. Outside the model of LED, a cylindrical magnetic field with a radius of 100 mm and a height of 160 mm was added along the $[001]$ direction. The magnetic field increased from 0 kA/m to 240 kA/m with the step of 1 kA/m . Fig. 2 shows the strain profiles in the active layer of $\text{Ge}_{0.92}\text{Sn}_{0.08}$ LED. Under the condition of 0 MPa pre-stress, the uniaxial tensile strains in ε_{zz} along $[001]$ direction were introduced into the active layer by the giant

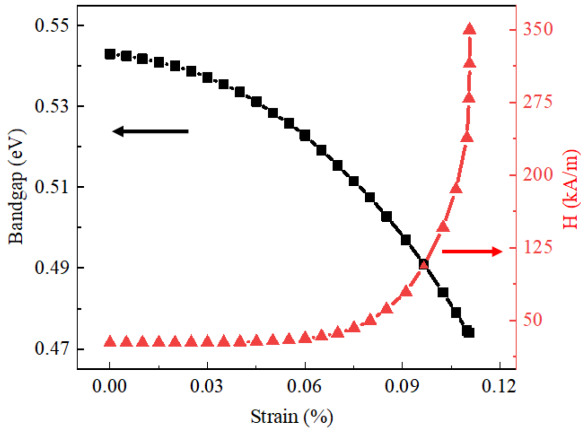


Fig. 3. Dependence of bandgap and magnetic field of $\text{Ge}_{0.92}\text{Sn}_{0.08}$ on strain in the active layer.

TABLE II
BAND PARAMETERS AT VARIOUS VALLEYS USED IN THE BAND ALIGNMENT CALCULATION

Valley	$E_{\text{Ge}}(\text{eV})$	$E_{\alpha\text{-Sn}}(\text{eV})$	$b_{\text{GeSn}}(\text{eV})$
L	0.66	0.14	0.68
Γ	0.795	-0.413	2.12

magnetostrictive stressor at $H = 50 \text{ kA/m}$ and $H = 240 \text{ kA/m}$ respectively shown in Fig. 2. An adjustable strain in the range of 0–0.11% can be obtained by adjusting the magnetic field strength as shown the red triangle marked line in Fig. 3.

B. Impacts of Tensile Strain on Energy Band Structure, Carrier Distribution and r_{sp} in $\text{Ge}_{0.92}\text{Sn}_{0.08}$

Calculation of energy band diagrams for the relaxed and strained GeSn was carried out by introducing the 3×3 strain matrix based on the first principles ignoring the magnetic field [40], [41]. The energy band parameters of Ge and α -Sn and the bowing parameters of GeSn at 300 K are listed as Table II [42], [43], [44], [45].

Under the external magnetic field, an adjustable bandgap from 0.543 eV to 0.475 eV of $\text{Ge}_{0.92}\text{Sn}_{0.08}$ was achieved own to the adjustable tensile strain as shown in Fig. 3. Fig. 4(a) depicts the energy band diagram of relaxed $\text{Ge}_{0.92}\text{Sn}_{0.08}$. In order to study the influence of stressor on the energy band diagrams, a plane rectangular coordinate system was built as shown in Fig. 2(b), and the points A, B and C from inside to the outside along the line of ll' corresponding to the strain values of 0.11%, 0.08% and 0.06% are selected as the examples, respectively. The energy band diagrams of A, B and C were shown in Fig. 4(b)–(d). Compared with the relaxed $\text{Ge}_{0.92}\text{Sn}_{0.08}$, the energy difference between the point L (E_L) and point Γ (E_Γ) of the conduction band in 0.11% strained $\text{Ge}_{0.92}\text{Sn}_{0.08}$ is increased about 0.023 eV, and the splitting is induced between heavy hole (HH) and light hole (LH) in the valence band. Under the 0.11% uniaxial tensile strain, the direct and indirect bandgap of $\text{Ge}_{0.92}\text{Sn}_{0.08}$ are decreased from 0.543 eV ($E_{G,\Gamma}$) to 0.475 eV ($E_{G,\Gamma(\text{LH})}$) and 0.573 eV ($E_{G,L}$) to 0.528 eV ($E_{G,L(\text{A})}$), respectively, due to the

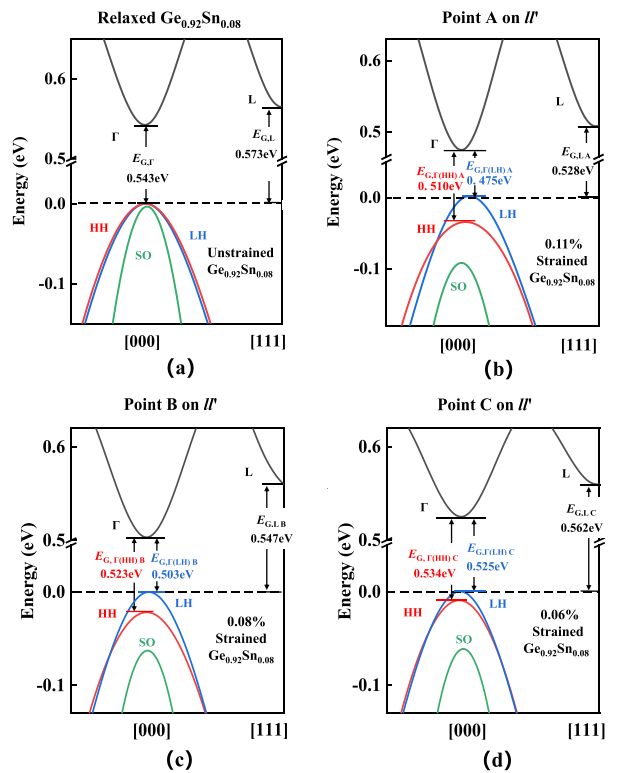


Fig. 4. Energy band diagrams of (a) relaxed $\text{Ge}_{0.92}\text{Sn}_{0.08}$, (b) 0.11% strained $\text{Ge}_{0.92}\text{Sn}_{0.08}$ at point A, (c) 0.08% strained $\text{Ge}_{0.92}\text{Sn}_{0.08}$ at point B and (d) 0.06% strained $\text{Ge}_{0.92}\text{Sn}_{0.08}$ at point C.

rise of LH and the decline of Γ valley. $E_{G,\Gamma}$ and $E_{G,L}$ decrease by 0.068 eV and 0.045 eV, respectively. The larger decrease of the $E_{G,\Gamma}$ than $E_{G,L}$ is caused by the Γ valley decreasing faster than the L valley under the uniaxial tensile strain. Besides, compared to the energy band diagrams of Fig. 4(b)–(d), the direct bandgap of strained $\text{Ge}_{0.92}\text{Sn}_{0.08}$ increases from inside to the outside along ll' due to decreasing strain.

The distribution of electrons in the Γ and L conduction valleys in GeSn directly affects the emitting efficiency of the devices. The increasing proportion of Γ conduction valley electrons in total electrons $n_{e,\Gamma}/n_{e,\text{total}}$ is beneficial to the improvement of the spontaneous radiation recombination of the device. Where $n_{e,\text{total}}$ equal to $n_{e,\Gamma} + n_{e,L}$. The electron concentrations in the Γ and L valleys can be obtained by using (1) [20]

$$n_{e,\Gamma(L)} = 8\sqrt{2\pi} \left(m_{e,\Gamma(L)}^* \cdot kT \right)^{3/2} / h^3 \cdot \int_0^\infty E^{1/2} / \{ 1 + \exp[E - (E_{fc} - E_{\Gamma(L)})/kT] \} \cdot dE \quad (1)$$

where $m_{e,\Gamma(L)}^*$ is the electron effective mass in Γ (L) valley, k is the Boltzmann constant, T is the temperature, h is the Plank constant, E_{fc} is the quasi-Fermi level for the conduction band. $E_{\Gamma(L)}$ is the energy at the bottom of Γ (L) valley, E is the energy of density of states for electrons. During the calculation, the E_{fc} of relaxed and tensile strained $\text{Ge}_{0.92}\text{Sn}_{0.08}$ alloys was scanned from 0.2 eV to 0.7 eV with the step of 0.0001 eV

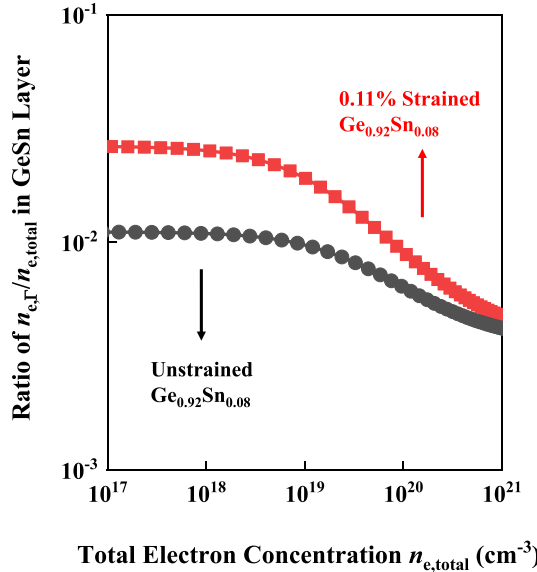


Fig. 5. $n_{e,\Gamma}/n_{e,\text{total}}$ in unstrained and 0.11% uniaxial tensile strained $\text{Ge}_{0.92}\text{Sn}_{0.08}$ LED.

[46]. Ratios of $n_{e,\Gamma}/n_{e,\text{total}}$ in unstrained and tensile strained $\text{Ge}_{0.92}\text{Sn}_{0.08}$ in LED are plotted in Fig. 5. Compared with unstrained $\text{Ge}_{0.92}\text{Sn}_{0.08}$, the $n_{e,\Gamma}/n_{e,\text{total}}$ achieves about 2.38 times higher in 0.11% uniaxial tensile strained $\text{Ge}_{0.92}\text{Sn}_{0.08}$ at the injected carrier density $1 \times 10^{17} \text{ cm}^{-3}$, due to a more pronounced drop in Γ conduction valley energy caused by tensile strain.

The spontaneous emission rate (r_{sp}) of the active layer in the GeSn LEDs integrated with the $\text{Tb}_{0.3}\text{Dy}_{0.7}\text{Fe}_{1.95}$ stressor was studied under different conditions. Due to the value of r_{sp} between the direct bandgap is much higher than that between the indirect bandgap, there only the photons induced by the electron transition from the Γ conduction valley to the valence band are considered. Ignoring the influence of the magnetic field, the value of r_{sp} per unit volume in the energy can be calculated by (2) [20]

$$r_{\text{sp}}(hv) = \left[8\sqrt{2}\pi^2 ne^2 v E_{G,\Gamma}(E_{G,\Gamma} + \Delta_{\text{so}}) m_r^{3/2} \right] / \left[3\varepsilon_0 h^4 c^3 m_e^* \times (E_{G,\Gamma} + 2\Delta_{\text{so}}/3) \right] \cdot (hv - E_{G,\Gamma})^{1/2} f_c(hv) f_v(hv) \quad (2)$$

where f_c and f_v are the Fermi factors for electrons and holes, respectively. The occupation probability f_c (f_v) of an electron (a hole) with energy E_{Γ} (E_v), f_c and f_v can be expressed as

$$f_c(hv) = 1/\exp \left[[(hv - E_{G,\Gamma})m_r/m_e^* - (E_{f_c} - E_{\Gamma})]/k_0 T \right] + 1 \quad (3)$$

and

$$f_v(hv) = 1/\exp \left[[(hv - E_{G,\Gamma})m_r/m_h^* - (E_v - E_{f_v})]/k_0 T \right] + 1, \quad (4)$$

respectively, where n is the refractive index, e is the elementary charge, v is the frequency of the photon, Δ_{so} is the spin-orbit

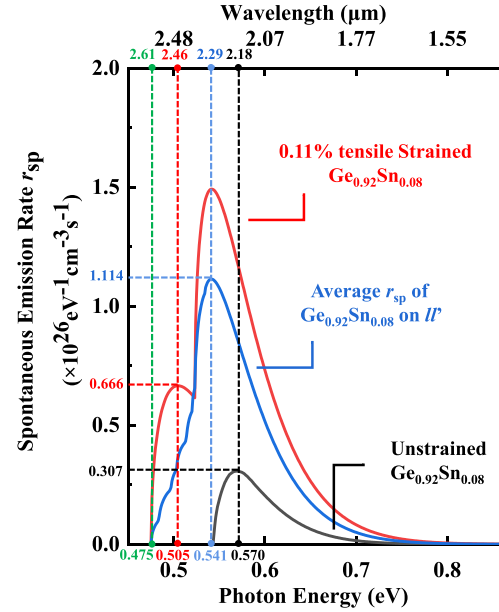


Fig. 6. Spontaneous emission rate and wavelength for the direct transition of LED under different states of strain.

splitting, ε_0 is the vacuum permittivity, m_r is the reduced mass. For the electron-heavy-hole transition, the $E_{G,\Gamma(\text{hh})}$, and the m_r are given by

$$E_{G,\Gamma(\text{hh})} = E_{\Gamma} - E_{\text{hh}} \quad (5)$$

and

$$m_r = m_e^* \cdot m_{\text{hh}}^* / (m_e^* + m_{\text{hh}}^*), \quad (6)$$

respectively.

Besides, for the electron-light-hole transition, the $E_{G,\Gamma(\text{lh})}$ and the m_r are given by

$$E_{G,\Gamma(\text{lh})} = E_{\Gamma} - E_{\text{lh}} \quad (7)$$

and

$$m_r = m_e^* \cdot m_{\text{lh}}^* / (m_e^* + m_{\text{lh}}^*), \quad (8)$$

respectively, where m_e^* is the effective mass of electrons, m_{lh}^* and m_{hh}^* are the effective mass of light-hole and heavy-hole, respectively.

In addition, the relationship between bandgap and light-emitting wavelength is obtained according to (9)

$$\lambda_0 = h \cdot c / E_p, \quad (9)$$

where E_p is the photon energy.

The spontaneous emission rate (r_{sp}) and the wavelength of relaxed $\text{Ge}_{0.92}\text{Sn}_{0.08}$, 0.11% uniaxial tensile strained $\text{Ge}_{0.92}\text{Sn}_{0.08}$ and the average of tensile strained $\text{Ge}_{0.92}\text{Sn}_{0.08}$ LED with a magnetostrictive strain source are shown in Fig. 6. There are two peaks in the calculated spontaneous emission rate of the 0.11% tensile strained $\text{Ge}_{0.92}\text{Sn}_{0.08}$, corresponding to the degenerated LH and HH, the peak of LH is located at 0.505 eV, corresponding to the wavelength of $2.46 \mu\text{m}$ and the value of peak is $0.666 \times 10^{26} \text{ eV}^{-1} \text{cm}^{-3} \text{s}^{-1}$, the peak of HH is located

at 0.541 eV, corresponding to the wavelength of 2.29 μm and the value of peak is $1.492 \times 10^{26} \text{ eV}^{-1}\text{cm}^{-3}\text{s}^{-1}$. The average spontaneous emission efficiency was obtained by integrating the spontaneous emission rate from inside to the outside along ll' . The average r_{sp} of $\text{Ge}_{0.92}\text{Sn}_{0.08}$ on ll' is lower than that of 0.11% strained $\text{Ge}_{0.92}\text{Sn}_{0.08}$ due to the nonuniform bandgap. In average r_{sp} , the peak is located at 0.541 eV, corresponding to the wavelength of 2.29 μm and the value of peak is $1.114 \times 10^{26} \text{ eV}^{-1}\text{cm}^{-3}\text{s}^{-1}$, which is 3.63 times higher than the peak of unstrained $\text{Ge}_{0.92}\text{Sn}_{0.08}$ caused by the smaller bandgap and the higher energy difference between E_L and E_Γ . The spontaneous emission peak of the average r_{sp} shows a redshift of 0.03 eV in comparison with the unstrained case due to the drop of Γ valley and the rise of LH. The adjustable peak luminous wavelength in SWIR can be extended from 2.18 μm with unstrained $\text{Ge}_{0.92}\text{Sn}_{0.08}$ to 2.46 μm with strained $\text{Ge}_{0.92}\text{Sn}_{0.08}$, and the boundary of luminous wavelength was extended to 2.61 μm .

IV. CONCLUSION

The strain-adjustable GeSn LEDs are investigated with giant magnetostrictive material $\text{Tb}_{0.3}\text{Dy}_{0.7}\text{Fe}_{1.95}$ filled in the active layer as the stressor. The range of 0–0.11% adjustable strain can be obtained by adjusting the magnetic field strength of 0–240 kA/m. With the adjusting of the magnetic field strength, the band structure of GeSn alloy can be changed purposefully to reduce the bandgap from 0.543 eV to 0.475 eV, adjustable range of luminous peak is achieved from 2.18 μm to 2.46 μm in SWIR. Analytical calculations show that a 3.63-fold enhancement of the spontaneous emission intensity of GeSn LEDs is achieved, which caused by the reduction of the bandgap and the increase in the proportion of Γ valley electrons $n_{e,\Gamma}/n_{e,\text{total}}$ tensile strain-induced of the GeSn active layer.

REFERENCES

- [1] B.-J. Huang et al., “Electrically injected GeSn vertical-cavity surface emitters on silicon-on-insulator platforms,” *ACS Photon.*, vol. 6, no. 8, pp. 1931–1938, 2019.
- [2] H.-J. Joo et al., “1D photonic crystal direct bandgap GeSn-on-insulator laser,” *Appl. Phys. Lett.*, vol. 119, pp. 1–6, 2021.
- [3] M. E. Kurdi et al., “Two-dimensional photonic crystals with pure germanium-on-insulator,” *Opt. Commun.*, vol. 281, no. 4, pp. 846–850, 2008.
- [4] I. Dascalescu et al., “Epitaxial GeSn obtained by high power impulse magnetron sputtering and the heterojunction with embedded GeSn nanocrystals for shortwave infrared detection,” *ACS Appl. Mater. Interfaces*, vol. 12, no. 30, pp. 33879–33886, 2020.
- [5] S. An, S. Wu, C. S. Tan, G.-E. Chang, X. Gong, and M. Kim, “Modulation of light absorption in flexible GeSn Metal–semiconductor–metal photodetectors by mechanical bending,” *J. Mater. Chem. C*, vol. 8, no. 39, pp. 13557–13562, 2020.
- [6] A. Gassend et al., “Gamma bandgap determination in pseudomorphic GeSn layers grown on Ge with up to 15% Sn content,” *Appl. Phys. Lett.*, vol. 109, 2016, Art. no. 242107.
- [7] L. Zhang et al., “High-Sn fraction GeSn quantum dots for Si-based light source at 1.55 μm ,” *Appl. Phys. Exp.*, vol. 12, 2019, Art. no. 055504.
- [8] S. Dev, K. R. Khiangte, and S. Lodha, “Wafer-scale mono-crystalline GeSn alloy on Ge by sputtering and solid phase epitaxy,” *J. Phys. D*, vol. 53, 2020, Art. no. 21LT01.
- [9] R. Chen, H. Lin, Y. Huo, C. Hitzman, T. I. Kamins, and J. S. Harris, “Increased photoluminescence of strain-reduced, high-Sn composition $\text{Ge}_{1-x}\text{Sn}_x$ Alloys grown by molecular beam epitaxy,” *Appl. Phys. Lett.*, vol. 99, 2011, Art. no. 181125.
- [10] C. Fang et al., “Germanium-tin alloys: Applications for optoelectronics in mid-infrared spectra,” *Optoelectron. Adv.*, vol. 1, no. 3, 2018, Art. no. 18000401.
- [11] M. R. M. Atalla, S. Assali, S. Koelling, A. Attiaoui, and O. Moutanabbir, “High-bandwidth extended-SWIR GeSn photodetectors on silicon achieving,” *ACS Photon.*, vol. 9, no. 4, pp. 1425–1433, 2022.
- [12] S. Golovynskyi et al., “Optical windows for head tissues in near-infrared and short-wave infrared regions: Approaching transcranial light applications,” *J. Biophoton.*, vol. 11, 2018, Art. no. e201800141.
- [13] J. Krieg and U. Adomeitvol, “Comparative long-time visible and short-wave infrared night illumination measurements,” *Appl. Opt.*, vol. 58, no. 36, pp. 9876–9882, 2019.
- [14] D. Buca et al., “GeSn for nanoelectronic and optical applications,” in *Proc. Joint Int. EUROSOI Workshop Int. Conf. Ultimate Integration Silicon*, 2015, pp. 157–160.
- [15] S. Gupta, B. Magyari-Köpe, Y. Nishi, and K. C. Saraswat, “Achieving direct band gap in germanium through integration of Sn alloying and external strain,” *J. Appl. Phys.*, vol. 113, 2013, Art. no. 073707.
- [16] G. Zhu, T. Liu, Z. Zhong, X. Yang, L. Wang, and Z. Jiang, “Fabrication of high-quality and strain-relaxed GeSn microdisks by integrating selective epitaxial growth and selective wet etching methods,” *Nanoscale Res. Lett.*, vol. 15, no. 1, pp. 1–7, 2020.
- [17] A. Bashir et al., “Strain analysis of a Ge micro disk using precession electron diffraction,” *J. Appl. Phys.*, vol. 126, 2019, Art. no. 235701.
- [18] W. Dou et al., “Investigation of GeSn strain relaxation and spontaneous composition gradient for low-defect and high-Sn alloy growth,” *Sci. Rep.*, vol. 8, 2018, Art. no. 5640.
- [19] D. Rainko et al., “Impact of tensile strain on low Sn content GeSn lasing,” *Sci. Rep.*, vol. 9, pp. 1–9, 2019.
- [20] Q. Zhang et al., “Theoretical analysis of performance enhancement in GeSn/SiGeSn light-emitting diode enabled by Si_3N_4 liner stressor technique,” *Appl. Opt.*, vol. 55, no. 34, pp. 9668–9674, 2016.
- [21] X. H. Liu, H. Zhang, X. L. Gao, and M. W. Chen, “Design and simulation analysis of giant magnetostrictive actuator,” *Mater. Technol.*, vol. 30, no. 3, pp. 155–158, 2014.
- [22] Z. Wang, J. Liu, C. Jiang, and H. Xu, “The stress-induced anisotropy in the (110) plane of the magnetostrictive TbDyFe [110] oriented crystal,” *J. Appl. Phys.*, vol. 108, 2010, Art. no. 063908.
- [23] C. Zhang, T. Ma, and M. Yan, “Induced additional anisotropy influences on magnetostriction of giant magnetostrictive materials,” *J. Appl. Phys.*, vol. 112, 2012, Art. no. 103908.
- [24] J. Zhang et al., “Enhancement of gyration effects by dysprosium-doped ferrite/piezoelectric magnetoelectric gyrators,” *IEEE Trans. Magn.*, vol. 58, no. 2, Feb. 2022, Art. no. 2500304.
- [25] J. Zhang et al., “Influence of shape on power conversion efficiency of Ni-Zn ferrite/piezoelectric magnetoelectric gyrator,” *J. Phys. Conf. Ser.*, vol. 1759, 2021, Art. no. 012007.
- [26] Q. Zhang, Y. Liu, J. Yan, C. Zhang, Y. Hao, and G. Han, “Theoretical investigation of tensile strained GeSn waveguide with Si_3N_4 liner stressor for mid-infrared detector and modulator applications,” *Opt. Exp.*, vol. 23, no. 6, pp. 7924–7932, Mar. 2015.
- [27] Q. Zhang, Y. Liu, C. Zhang, Q. Huang, Y. Hao, and G. Han, “Tensile-strained mid-infrared GeSn detectors wrapped in Si_3N_4 liner stressor: Theoretical investigation of impact of device architectures,” *IEEE Photon. J.*, vol. 7, no. 6, Dec. 2015, Art. no. 6803208.
- [28] R. W. Millar et al., “Mid-infrared light emission >3 microm wavelength from tensile strained GeSn microdisks,” *Opt. Exp.*, vol. 25, no. 21, pp. 25374–25385, 2017.
- [29] H. Yang et al., “Influence of top surface passivation on bottom-channel hole mobility of ultrathin SiGe- and Ge-on-insulator,” *Appl. Phys. Lett.*, vol. 93, 2008, Art. no. 072104.
- [30] H.-S. Lee and C. Cho, “Study on advanced multilayered magnetostrictive thin film coating techniques for MEMS application,” *J. Mater. Process. Technol.*, vol. 201, no. 1, pp. 678–682, 2008.
- [31] M. Yang, J. Dai, C. Zhou, and D. Jiang, “Optical fiber magnetic field sensors with TbDyFe magnetostrictive thin films as sensing materials,” *Opt. Exp.*, vol. 17, no. 23, pp. 20777–20782, 2009.
- [32] S. Daniela et al., “Short-wave infrared LEDs from GeSn/SiGeSn multiple quantum wells,” *Optica*, vol. 4, no. 2, pp. 185–188, 2017.
- [33] H. Kumar, R. Basu, and G. - E. Chang, “Impact of temperature and doping on the performance of $\text{Ge}/\text{Ge}_{1-x}\text{Sn}_x/\text{Ge}$ heterojunction phototransistors,” *IEEE Photon. J.*, vol. 12, no. 3, Jun. 2020, Art. no. 6801814.
- [34] P. Westwood, J. S. Abell, and K. C. Pitman, “Phase relationships in the Tb-Dy-Fe ternary system,” *J. Appl. Phys.*, vol. 67, no. 9, pp. 4998–5000, 1990.

- [35] M. Palit, S. Pandian, and K. Chattopadhyay, "Phase relationships and magnetic properties of $Tb_xDy_{1-x}Fe_{1.95}$ Alloys," *J. Alloys Compounds*, vol. 541, pp. 297–304, 2012.
- [36] Z. Deng and M. J. Dapino, "Review of magnetostrictive materials for structural vibration control," *Smart Mater. Struct.*, vol. 27, no. 11, pp. 1–18, 2018.
- [37] Y. Pei and D. Fang, "Experimental study of the multiaxial ferroelastic behavior of $Tb_{0.3}Dy_{0.7}Fe_{1.95}$ alloys," *Smart Mater. Struct.*, vol. 17, no. 06, pp. 1–6, 2008.
- [38] S. Adachi, *Properties of Semiconductor Alloys*. New York, NY, USA: Wiley, 2009.
- [39] T. Speliotis and D. Niarchos, "Extraordinary magnetization of amorphous TbDyFe films," *Microelectron. Eng.*, vol. 112, pp. 183–187, 2013.
- [40] W. Huang, B. Cheng, C. Xue, and Z. Liu, "Comparative studies of band structures for biaxial (100), (110), and (111) strained GeSn: A first-principles calculation with GGA+U approach," *J. Appl. Phys.*, vol. 118, no. 16, pp. 1–7, 2015.
- [41] S. Sun, W. Huang, L. Zhang, Z. Chen, H. Wang, and C. Zhang, "Band and luminescence regulation of SiGeSn ternary alloy: A first-principles investigation," *J. Alloys Compounds*, vol. 899, pp. 1–5, 2022.
- [42] G. Sun, R. A. Soref, and H. H. Cheng, "Design of an electrically pumped SiGeSn/GeSn/SiGeSn double-heterostructure midinfrared laser," *J. Appl. Phys.*, vol. 108, no. 3, pp. 1–3, 2010.
- [43] D. Rainko et al., "Investigation of carrier confinement in direct bandgap GeSn/SiGeSn 2D and 0D heterostructures," *Sci. Rep.*, vol. 8, no. 1, pp. 1–13, 2018.
- [44] M.-Y. Ryu, T. R. Harris, Y. K. Yeo, R. T. Beeler, and J. Kouvetakis, "Temperature-dependent photoluminescence of Ge/Si and $Ge_{1-y}Sn_y/Si$, indicating possible indirect-to-direct bandgap transition at lower Sn content," *Appl. Phys. Lett.*, vol. 102, 2013, Art. no. 171908.
- [45] N. Driesch et al., "Epitaxy of direct bandgap group IV Si-Ge-Sn alloys towards heterostructure light emitters," *ECS Trans.*, vol. 86, no. 7, pp. 189–197, 2018.
- [46] B. Dutt et al., "Theoretical analysis of GeSn alloys as a gain medium for a Si-compatible laser," *IEEE J. Sel. Topics Quantum Electron.*, vol. 19, no. 5, Sep./Oct. 2013, Art. no. 1502706.